The effect of substrate conduction on boiling data on pin-fin heat sinks

D A McNeil[1+], A H Raeisi[2], P A Kew[1] and R S Hamed[1]

1. School of Engineering and Physical Science, Heriot-Watt University, UK

2. School of Engineering and Design, Brunel University, UK

+ Corresponding author Email: D.A.McNeil@hw.ac.uk

Abstract

Heat-transfer experiments for a copper heat sink containing pin-fins with a cross section of 1 mm by 1 mm and a height of 1 mm have been reported previously. The pin-fins were manufactured on a 5 mm thick, 50 mm square base plate in a square, in-line arrangement with a pitch of 2 mm. Data were produced while boiling R113 and water at atmospheric pressure.

The heat sink was heated from below through a 5 mm thick aluminium wall by an electrical heating method that is normally associated with the uniform heat flux boundary condition. However, variations in the heat-transfer coefficient and the liquid subcooling interacted with the high thermal conductivity of the aluminium and copper materials to produce a near isothermal wall boundary condition. Thus, heat conduction effects had to be taken into account when determining the heat-flux distribution required in the analysis of the data. Many experiments like these have used the uniform heat-flux assumption to analyse the data. The discrepancies produced from this approach are explored.

Single-phase flows across a pin-fin surface produce a reasonably uniform distribution of heat-transfer coefficient. However, the liquid temperature increases as it moves across the heat sink. This produces a non-uniform heat flux distribution at the solid-fluid interface. The uniform heat-flux assumption is shown to lead to errors of ±17% in the estimation of the heat-transfer coefficient.

The original boiling flow experiments found that the water data were confined and that the majority of the R113 data were not. The confined and unconfined data are processed with the thermal conduction in the walls taken into account and by assuming a uniform heat flux at the solid-fluid interface. The uniform heat-flux distribution analysis for unconfined flows shows errors in the heat-transfer coefficient to be typically ±17%. Confined flows produce smaller errors, typically ±12%, close to the onset of nucleation. However, these damp out as the distance from the onset increases.

The effect of test-section design is investigated by repeating the analyses with smaller wall thickness and lower wall thermal conductivities. Lower wall thermal conductivity is shown to produce a uniform heat flux distribution at the expense of reduced extended surface effectiveness. Thinner substrate thicknesses are found to give limited improvements.

These analyses demonstrate that an applied uniform heat flux to the heat sink base will not result in a uniform heat flux at the solid-liquid interface.

1.0 Introduction

Flow boiling in mini- and micro-flow passages can be used for cooling many high power devices such as Micro Electro Mechanical Systems (MEMS), microprocessors and laser diode arrays. This has led to many experimental studies of boiling in small-scale flow passages. Many of these experimental studies have used Joule heating to produce the applied heat flux, which is usually assumed to be uniform at the solid-liquid interface. Recent studies have questioned the universality of this assumption. McNeil et al [1] analysed data from a heat sink containing 1 mm square parallel mini-channels with the heat sink heated from below by a uniform heat flux. They, in common with many researchers, used a subcooled liquid at the heat-sink inlet. This led to single-phase, subcooled boiling and saturated boiling heat-transfer occurring on the heat sink, frequently simultaneously. The variation in heat-transfer coefficient across the heat sink induced by phase change and the variation in liquid temperature produced a non-uniform heat flux at the solid-fluid interface. McNeil et al [2] produced similar results for water and R113 boiling on a pin-fin surface. Szczukiewicz et al [3] reported on work carried out with infra red cameras that measured wall temperature distributions on surfaces heated by a uniform heat flux. They also found that subcooled liquid at heat sink inlets caused a heat flux distortion that required conduction in the substrate to be taken into account in the analysis of the data.

This study uses data reported by McNeil et al [2, 4] to investigate the effects of substrate conduction. This data was chosen because the R113 data [4] and the water data [2] were obtained from experiments on the same substrate and the R113 data were found, in the main, not to be confined, where as the water data were found to be confined. Thus, these data allow different types of heat-flux distortion to be explored. This is achieved by using the models produced from the analysis of these data [2] to produce ‘actual’ data for the heat sink. ‘Measured’ data is produced by applying the uniform heat-flux data reduction technique so that errors due to this technique can be found. The alternative modelling method of uniform wall superheat is also explored.

2.0 Test section

How the experimental data were obtained is detailed in [2] and [4]. However, to understand how heat conduction was significant, the test section is reproduced in Figure 1. Liquid entered the inlet plenum of the test-section through the two inlet ports set at 90^o to the direction of flow through the heat sink. The plenum chamber dimensions were set to reduce the liquid velocity to close to zero before it accelerated into the settling length upstream of the heat sink. The fluid boiled as it passed across the heat sink. Heat was supplied to the heat sink from a ceramic heater. The heater was 50 mm square and was placed below the test piece. The heater was fixed to the test section by a securing plate. A PTFE block was located between the securing plate and the heater to minimize heat transfer from the lower surface of the heater. Power to the heater was adjusted to give the required heat flux.

The heat sink is shown in Figure 2. It was constructed from a piece of copper, 50 mm wide by 50 mm long and 6 mm high. The channels were formed by cutting slots 1 mm wide and 1 mm deep in the longitudinal and translational directions. The slots were 1 mm apart. Holes, 0.6 mm in diameter and 12.5 mm long, were drilled into the heat sink at the inlet and outlet ends. The holes were located 2.5 mm from the top of the boiling surface and 11 and 39 mm from an edge. These holes allowed sheathed K-type thermocouples, 0.5 mm in diameter, to be located below the boiling surface to estimate local wall temperatures.

3.0 Heat transfer and fluid flow model

The model derived to explain the experimental data reported in [2] and [4] had three components, a flow model, a heat-transfer model and a wall conduction model. These three models were linked because the heat flux applied to the base of the heat sink had to conduct through it and pass to the fluid through the extended surface of the pin fins. The heat-transfer coefficient at the surface depended on the fluid flow conditions in the heat sink and was flow regime dependent. A reasonable simulation of the experiments was achieved by solving these three models together. This model is taken to describe what actually occurred in the heat sink.

3.1 Flow model

Two-phase flow was observed while subcooled boiling was taking place. The simplest way to mimic this behaviour was to have a channel through the heat sink that could contain single-phase, growing slug, frozen slug and saturated flows placed above the conducting wall depicted in Figure 3. An energy balance for an element of the heat sink that allows for all of these possibilities gives

$$q_b W = (1-x) M c_p \frac{dT_L}{dz} + M\left[c_p(T_{sat} - T_L) + h_{fg}\right]\frac{dx}{dz} \qquad (1)$$

where q_b is the local base heat flux at the solid-fluid interface, x is the gas-mass fraction, W is the width of the heat sink, M is the mass flow rate through the heat sink, c_p is the specific heat capacity of the liquid, T_L is the liquid temperature, T_{sat} is the saturation temperature, h_{fg} is the enthalpy of evaporation and z is the ordinate in the flow direction. Subcooled liquid entered the heat sink and remained liquid until the onset of nucleation. The single-phase liquid temperature was therefore found from Equation (1) for a constant gas-mass fraction of zero, i.e.

$$q_b W = M c_p \frac{dT_L}{dz} \tag{2}$$

The end of the single-phase region was concurrent with the onset of the growing slug regime, which occurred at the onset of nucleation. The onset of nucleate boiling was taken to occur when the criterion of Sato and Matsumura [5] was achieved, i.e.

$$q_s = \frac{k_L h_{fg} \rho_V (T_w - T_{sat})^2}{8 \sigma T_{sat}} \tag{3}$$

where k_L is the liquid thermal conductivity, ρ_V is the vapour density, σ is the surface tension, T_w is the wall temperature and q_s is the local surface heat flux at the solid-fluid interface. In the growing slug region it was assumed that all of the added energy resulted in slug growth, implying that the liquid temperature was constant and that the gas-mass fraction could be found from Equation (1) as

$$q_b W = M\left[c_p (T_{sat} - T_L) + h_{fg}\right] \frac{dx}{dz} \tag{4}$$

The growing slug regime was assumed to continue until bubble coalescence occurred at a critical void fraction. The frozen slug regime followed the growing slug regime and was characterized by a constant gas-mass fraction. In this regime, the liquid temperature was the solution of the reduced form of Equation (1),

$$q_b W = (1 - x_T) M c_p \frac{dT_L}{dz} \tag{5}$$

where x_T is the gas-mass fraction corresponding to the critical void fraction. The frozen slug regime continued until the liquid temperature reached the saturation value, whence Equation (1) allowed the gas-mass fraction to be found from

$$q_b W = M h_{fg} \frac{dx}{dz} \tag{6}$$

The pressure distribution in a channel through the heat sink was obtained from the integration of the pressure gradient, dp/dz, given by

$$\frac{dp}{dz} = \left(\frac{dp}{dz}\right)_A + \left(\frac{dp}{dz}\right)_F \tag{7}$$

where $(dp/dz)_A$ is the pressure gradient due to acceleration and $(dp/dz)_F$ is the pressure gradient due to friction. The acceleration pressure gradient was determined from the homogeneous flow model, i.e.

$$\left(\frac{dp}{dz}\right)_A = -\left(\frac{M}{A}\right)^2 \frac{dv_H}{dz} \tag{8}$$

where A is the total flow area between the pin-fins and v_H is the homogeneous specific volume, found from

$$v_H = x v_V + (1 - x) v_L \tag{9}$$

in which v_V and v_L are the specific volumes of vapour and liquid phases respectively. The frictional pressure gradient was set to zero for water, [2], and was obtained for R113 from the two-phase multiplier method, i.e.

$$\left(\frac{dp}{dz}\right)_F = -\frac{f_L}{2D\rho_L}(1-x)^2 \left(\frac{M}{A}\right)^2 \phi_L^2 \tag{10}$$

The single-phase friction factor, f_L, was found from the method of ESDU [6]. The two-phase multiplier, ϕ_L^2, was given by the method of Ishihara et al [7], i.e.

$$\phi_L^2 = 1 + \frac{8}{X} + \frac{1}{X^2} \tag{11}$$

where the Martinelli parameter, X, was found from

$$X = \left(\frac{1-x}{x}\right)^{0.9} \sqrt{\frac{\rho_V}{\rho_L}} \left(\frac{\mu_L}{\mu_V}\right)^{0.1} \tag{12}$$

in which μ_L and μ_V are the liquid and vapour viscosities respectively.

3.2 Heat-transfer model

The liquid entered the heat sink in a subcooled state. Three heat-transfer mechanisms were therefore possible, single-phase convection, subcooled boiling and saturated boiling. The model allowed for all three mechanisms.

The heat moves from the base of the heat sink, Figure 3, through its surface and into the fluid through two heat flow paths. The first path was through the base of the heat sink and the second was through the walls of the pin-fins. These paths allowed the fin efficiency approach to be used. A one-dimensional heat balance through a repeating pitch of flow length at the base of the heat sink gave

$$q_b (W_{ch} + W_w)^2 = \left[\alpha_{cv}(T_w - T_L) + \alpha_{nb}(T_w - T_{sat})\right]\left[(W_{ch} + W_w)^2 - W_w^2 + 4\eta W_w H_{ch}\right] \tag{13}$$

where α_{cv} is the convective heat-transfer coefficient, α_{nb} is the nucleate boiling heat-transfer coefficient, η is the fin efficiency, W_{ch} is the channel width between the pin fins, W_w is the width of a pin-fin and H_{ch} is the height of a pin-fin.

The fin efficiency was found by assuming that the fins could be treated as rods with no heat transfer from their tips, i.e.

$$\eta = \frac{\tanh(\lambda H_{ch})}{\lambda H_{ch}} \tag{14}$$

where λ was the fin parameter, given by

$$\lambda = \sqrt{\frac{4(\alpha_{cv} + \alpha_{nb})}{k W_w}} \tag{15}$$

in which k is the thermal conductivity of copper. The derivation of Equation (15) assumes that the nucleate boiling, heat-transfer coefficient is constant along the length of a pin. This is an approximation as it varies with wall superheat and therefore with position on the pin-fin. The nucleate boiling heat-transfer coefficient was evaluated at the base wall superheat.

Below the onset of nucleation, as described by Equation (3), heat transfer was by single-phase convection. The single-phase heat-transfer coefficient, α_{sp}, was correlated by

$$\alpha_{sp} = 0.0592 \frac{k_L}{D_t} (Re_L Pr_L)^{0.726} \tag{16}$$

where Re_L is the liquid Reynolds number, Pr_L is the liquid Prandtl number and D_t is the thermal diameter for a passage heated on three sides. As the local heat flux increased, the onset of nucleation occurred when the single-phase convective heat flux balanced with that given by Equation (3), i.e.

$$q_s = \frac{k_L h_{fg} \rho_G (T_w - T_{sat})^2}{8 \sigma T_{sat}} = \alpha_{sp} \left(\triangle T_{sup} + \triangle T_{sub} \right) \tag{17}$$

where ΔT_{sup} is the local wall superheat and ΔT_{sub} is the local liquid subcooling.

Equation (17) either located the onset of nucleation somewhere between the inlet and outlet of the heat sink, or it demonstrated that nucleation occurred at the heat-sink inlet. In either case a slug inception model was used. The slug inception model moved the heat-transfer mode from single-phase flow through boiling bubbly flow and into boiling slug flow over a finite length. This process involved rapid changes in the heat-transfer coefficient that led to rapid changes in heat flux. These changes could take place at scales incompatible with the heat-conduction mesh, Figure 3. Values from the slug inception length were therefore ‘smoothed’ onto the conduction mesh to allow these rapid changes to interact with heat conduction in the copper substrate.

The convective heat-transfer coefficients for bubbly and slug flows were obtained from

$$\alpha_{cv} = E_{sf} \alpha_{sp} \tag{18}$$

Homogeneous flow was assumed, allowing the bubbly and slug flow enhancement factors, E_{sf}, to be given by

$$E_{sf} = \left(\frac{v_H}{v_L} \right)^{0.726} \tag{19}$$

The heat fluxes removed by convective and nucleate boiling were averaged over a surface element. The surface to fluid heat flux therefore balanced as,

$$q_s = q_{cv} + q_{nb} \tag{20}$$

The nucleate boiling heat transfer coefficient was assumed to follow a power-law relationship with surface heat flux, i.e.

$$q_{nb} = \alpha_{nb}\Delta T_{sup} = \beta q_{nb}^{n}\Delta T_{sup} \tag{21}$$

This allows Equation (20) to be re-cast as

$$\alpha_{cv}\left(\Delta T_{sup} + \Delta T_{sub}\right) + \left(\beta\Delta T_{sup}\right)^{\frac{1}{(1-n)}} - q_s = 0 \tag{22}$$

The Cooper correlation [8] was used to determine the nucleate boiling heat-transfer coefficient. This correlation has an index, *n*, of 0.67 and a coefficient , β, given by

$$\beta = \frac{55}{M_w^{0.5}} P_r^{\left(0.12-0.4343 ln\left(R_p\right)\right)}\left(-0.4343\ ln(\ P_r)\right)^{-0.55} \tag{23}$$

where P_r is the reduced pressure, R_p is the surface roughness in μm and M_w is the molecular weight. The surface roughness parameter was chosen to remove surface roughness dependency.

Following the slug inception length, slug flow existed in a subcooled liquid with the slug flow heat-transfer coefficient evaluated at the gas-mass fraction corresponding to the critical void fraction. For water [2], the heat-transfer coefficient downstream of the slug inception length remained constant. For R113 [2], it remained constant until saturated flow occurred, whence it moved from the slug to the annular flow value. In all cases Equation (22) was used to describe the heat-transfer processes.

The R113 data were found not to be confined and therefore followed a macro-scale heat transfer process. The process was flow pattern dependent. The transition from bubbly to slug flow required a critical void fraction to be set. A value of 0.25 was used to be consistent with the flow maps of Taitel et al [9]. Additionally, the Taitel et al [9] critical Martinelli parameter of 1.6 was used for the transition from intermittent to annular flow. These flow pattern transitions separated the convective heat-transfer into three regimes, bubbly flow, intermittent flow and annular flow. In the bubbly flow regime, Equation (18) was used for the heat-transfer coefficient. In the annular flow regime it was determined from

$$\alpha_{cv} = E_{af}\alpha_{spo} \tag{24}$$

where α_{spo} is the single-phase value, determined from Equation (16) using the liquid-only flow. The annular flow enhancement factor, E_{af}, was given by

$$E_{af} = 1 + \frac{0.914}{X^{0.814}} \tag{25}$$

In the intermittent flow regime, the convective heat-transfer coefficient was obtained from a linear interpolation along the gas-mass fraction line between the slug and annular flow values. The slug heat-transfer coefficient corresponded to the bubbly regime value, evaluated at the critical void fraction.

The water data were found to be confined and the heat-transfer coefficient was found to be reasonably constant across the length of the heat sink. The heat-transfer coefficient was therefore reasonably insensitive to local conditions. At low heat flux, the heat-transfer coefficient depended on the critical void fraction achieved at the exit from the slug inception length. At high heat flux it depended on the superficial gas velocity. The low heat flux data were correlated by

$$x_T = 433 B_N^{1.54} \tag{26}$$

where B_N is the Boiling number, defined as

$$B_N = \frac{q_B}{m h_{fg}} \tag{27}$$

where q_B is the heat flux applied at the base and m is the mass flux based on the flow area of the passages between the pin-fins. The high heat flux data were independent of Boiling number and achieved a constant value at a critical superficial gas velocity of 1.21 m/s ± 15%. At mid-range heat fluxes, the data diverged from the low heat-flux data at a critical void fraction of about 0.83 ± 3%, corresponding to a critical gas-mass fraction of 0.0031, before arriving at the high values corresponding to the critical superficial gas velocity. They therefore varied with Boiling number and mass flux. However, for each mass flux, these data were be correlated by

$$x_T = \gamma B_N^m \tag{28}$$

These characteristics are consistent with slug flow at low Boiling numbers, annular flow at high Boiling numbers and elongated slug flow in between these extremes. However, the flow pattern depended on the conditions at the end of the slug inception length and not the local conditions. These critical void fractions are significantly larger than those found in unconfined flows.

3.3 Wall conduction model

The geometry of the test section has two plates sandwiched between the fluid and the ceramic heater, an aluminium plate and the copper heat sink, both 50 mm square and 5 mm thick, Figure 1. This geometry will only produce a uniform heat flux distribution at the solid-fluid interface if the heat-transfer coefficient and temperature are reasonably constant. This was not the case. The heat-conduction through the walls was therefore incorporated into the analysis.

The temperature variation across the width of the heat sink was found to be insignificant. The dominant wall conduction effect was therefore assumed to be two-dimensional, with one-dimension parallel to the fluid flow and the other perpendicular to it, Figure 3. The heat-conduction equation is

$$\frac{\partial^2 T}{\partial y^2} + \frac{\partial^2 T}{\partial z^2} = 0 \tag{29}$$

where T is the temperature in the copper or aluminium walls and y is the ordinate perpendicular to the flow. McNeil et al [1] analysed data from the same test section for a parallel channel heat sink. They found that Equation (29) could be solved to sufficient accuracy by sub-dividing the area into 1 mm square cells. For each cell, Figure 3, an energy balance gave

$$T_{i,j} = \frac{\Delta y^2 (T_{i+1,j} + T_{i-1,j}) + \Delta z^2 (T_{i,j+1} + T_{i,j-1})}{2(\Delta y^2 + \Delta z^2)} \tag{30}$$

where Δy and Δz were the cell dimensions. Equation (30), and the variants of it necessary to implement the boundary conditions shown in Figure 3, were solved iteratively until the relative temperature in each cell was the same as the previous estimate to within a relative error of 0.0003. The wall temperatures were solved relative to the liquid inlet temperature so that temperature differences could be obtained accurately. Heat-flux continuity was enforced at the aluminium-copper interface.

3.4 Solving information

The physical properties of the fluids were evaluated at the temperature and pressure at the centre of each of the fifty segments required by the heat conduction model, Figure 3, and were assumed constant throughout each segment.

The solution was found by firstly determining the applied base heat flux necessary to produce a single-phase solution with the onset of nucleation occurring at the heat sink exit. If the actual applied base heat flux was less than this, the solution was single-phase. The minimum applied base heat flux required to produce fully-developed boiling from the heat sink inlet was then determined. If the actual applied base heat flux was greater than this, a solution with fully-developed boiling from the heat sink inlet was obtained. If the actual applied base heat flux was less than this, a solution involving single-phase and two-phase flow on the heat sink was obtained.

Solutions were obtained by estimating the wall superheat. The Energy equation was then used to obtain the local fluid conditions and the distribution of the heat-transfer coefficient. These local properties were fed into the boundary conditions of the heat-conduction equation, which was solved to update the wall superheat distribution. The process was repeated until the relevant quantities converged.

4.0 Generating synthetic uniform heat flux data

The model described in Section 3 was used to produce 'actual' values of the heat-transfer coefficient distributions, heat-flux distributions, fluid flow properties and wall temperature distributions. The same set-up was analysed using the uniform heat flux assumption to produce synthetic 'measured' values. The difference between the actual and measured values is therefore caused by the analysis assumption only. The 'measured' values are produced using a typical data reduction technique that involves measuring wall temperatures below the surface, projecting them to the surface using the one-dimensional heat conduction equation, determining the local fluid conditions from an energy balance and determining the local heat-transfer coefficient from the local wall and fluid temperatures.

Thermocouples were located within the heat sink 2.5 mm below the top of the heat sink surface, Figure 2. They were located 12.5 mm from the inlet and 12.5 mm from the outlet. These are hereafter referred to as the inlet and outlet locations. The 'measured' local wall temperature, T_m, at these locations was taken from the 'actual' values, produced from the model described in Section 3. As is common practice, the 'measured' wall temperatures at the surface were obtained by correcting these 'measurements' for their depth from the fluid-solid interface through the one-dimensional heat-conduction equation, i.e.

$$T_w = T_m - \frac{\Delta y_{tc} q_B}{k} \tag{31}$$

where Δy_{tc} is the depth of the measurement location from the solid-fluid interface.

The energy equation was used to estimate the local 'measured' conditions. The liquid temperature was obtained from

$$T_L = T_{in} + \frac{W q_B}{M} \int_0^z \frac{1}{c_p} dz \tag{32}$$

where T_{in} is the liquid inlet temperature. Saturated flow occurred when the liquid temperature reached the local saturation value. This occurs at a distance of L_{sp} from the heat sink inlet. Thereafter, the gas-mass fraction was found from

$$M h_{fg} x = q_B W \left(z - L_{sp}\right) \tag{33}$$

The pressure drop model described in Section 3 was used to obtain the saturation temperature. These 'measured' values were used in Equation (13) to obtain the 'measured' heat-transfer coefficients.

5.0 The effect of substrate conduction on single-phase flows

The distribution of typical heat-transfer parameters for a single-phase liquid flow through the heat sink are shown in Figure 4. The predictions from the model outlined in Section 3 are classified as the actual values. The actual heat-

transfer coefficient is constant across the heat sink, Figure 4a. Heat conduction in the substrate produces a relatively small wall temperature variation, Figure 4c. However, the liquid is colder at the heat-sink inlet, Figure 3d, so that the heat-flux is larger at the inlet and decreases as the fluid temperature increases as the fluid moves across the heat sink, Figure 4b. The actual heat-flux distribution is significantly different to the uniform heat-flux value, being 40% above at the heat-sink inlet and 31% below at the outlet. The uniform heat-flux analyses used the actual wall temperatures to determine the heat-transfer coefficient. Thus, the inaccurate liquid temperatures and heat fluxes led to the distribution of 'measured' heat-transfer coefficient shown in Figure 4a, where the measured values are 29% below the actual value at the heat-sink inlet, rising to 46% above it at the heat-sink outlet.

The 'measured' values produced at the inlet and outlet thermocouple locations by the method outlined in Section 4 are compared with the actual values in Figure 5. The data were obtained at the test conditions used in the original experiments. Thus, this figure depicts the errors that would have been made in the measurements had a uniform heat-flux analysis been used. The heat-flux distribution, Figure 5a, contains error bars that show the deviation of the actual results from the uniform heat-flux values. These are the root mean square (rms) deviations for the data sets and are ±21% for R113 and ±26% for water, with the relative differences being larger at the lower heat fluxes. The rms errors based on the deviation of the uniform heat-flux values from the actual values are ±24% and ±32% for R113 and water respectively. However, the errors are position dependent. For R113 the heat flux is underestimated by 17% at the inlet thermocouple location and overestimated by 29% at the outlet location. For water the heat flux is underestimated by 19% at the inlet thermocouple location and overestimated by 41% at the outlet location. The distortion to the wall temperature is not significant, Figure 5b, indicating that one-dimensional heat-conduction correction is not a major source of error. However, estimating the liquid temperature by this method does produce significant errors, Figure 5c. The constant heat-flux analysis produced rms errors in the heat-transfer coefficient of ±20% and ±24% for R113 and water respectively. However, these were again location dependent with R113 values underestimated by 23% at the inlet thermocouple location and overestimated by 17% at the outlet location while water values were underestimated by 30% at the inlet thermocouple location and overestimated by 15% at the outlet location. These errors also increase as the mass flux decreases, Figure 5d.

6.0 The effect of substrate conduction on macro-scale boiling flows

Macro-scale flows were obtained by boiling R113 flows across the heat sink. Examples of the distributions of boiling parameters predicted by the model are shown in Figure 6. At the lowest heat flux of 6.7 kW/m^2, the flow is single-phase throughout, resulting in a constant heat-transfer coefficient, Figure 6a, a declining heat flux, Figure 6b, near constant wall temperature, Figure 6c and zero void fraction, Figure 6d. With increasing heat flux,

slugs develop in the first few millimetres of the heat sink, as depicted by the increase in void fraction from 0 to 0.25 in Figure 6d. These slugs generate constant heat-transfer coefficients in subcooled liquid with increasing values in the saturated region, Figures 6a. The wall temperatures remain reasonably constant at heat-fluxes below 136 kW/m^2, Figure 6c, with the temperature difference across the heat sink being less than 1 K. This gives the relatively minor, but still significant, distortions to the heat flux distributions shown in Figure 6b. These distortions arise mainly from the onset of nucleation. At a heat flux of 136 kW/m^2, a major distortion occurs in the heat-flux distribution, Figure 6b, as heat is drawn to the heat-sink outlet by the high heat-transfer coefficients, Figure 6a, caused by the increase in gas-mass fraction. Figure 6b also shows the average applied heat flux, corrected for actual area and fin efficiency. The lines are of the same type as the actual distributions and are in grey. At larger heat fluxes, the wall temperature variation becomes significant, Figure 6c, emphasising the effect of lateral conduction in the substrate.

Typical distribution of heat-transfer and fluid flow parameters at the inlet and outlet thermocouple locations are shown for a constant mass flux and variable heat flux in Figure 7. The ‘measured’ values were obtained by assuming uniform heat flux. The ‘actual’ values were obtained from the model described in Section 3. The wall superheat is shown to be in good agreement, Figure 7a, suggesting that the one-dimensional heat-conduction correction is not a major source of error. The heat-flux distribution, Figure 7b, contains error bars set at ±11%. These show the rms deviation of the model from the uniform heat flux values. The heat flux at the inlet thermocouple location is underestimated at low heat flux and overestimated at high heat flux. The opposite occurs at the outlet thermocouple location. The void fraction distributions are in good agreement at the outlet thermocouple where thermodynamic equilibrium is prevalent, Figure 7c. However, the effect of non-equilibrium is more pronounced at the inlet thermocouple. These factors combine to produce the distortion to the heat-transfer coefficients shown in Figure 7d. The uniform heat-flux values deviate from the actual values with an rms error of ±17%. The heat-transfer coefficient at the inlet thermocouple location is underestimated at low heat flux and overestimated at higher values. The reverse occurs at the outlet thermocouple location. Overall, the uniform heat flux assumption reduces the difference between the two values.

Comparisons of ‘measured’ and ‘actual’ values are shown in Figure 8. These show that the single mass-flux results depicted in Figure 7 are repeated across the range. The one-dimensional heat-conduction correction produced a negligible error in the wall superheat, Figure 8a. The heat flux at the inlet wall thermocouple location is, in the main, systematically underestimated at low heat flux and systematically overestimated at higher values, Figure 8b. The rms error is ±12%. The opposite occurs at the outlet thermocouple location, where the rms error is

again ±12%. The void fraction prediction shows larger errors the closer to the inlet that the comparison is made, Figure 8c. The heat-transfer coefficient is shown to be systematically in error, with values at the inlet thermocouple location being overestimated by typically ±21% and values at the outlet being underestimated by typically ±13%, Figure 8d, giving an error of ±17% for the data set.

7.0 The effect of substrate conduction on micro-scale boiling flows

Micro-scale flows were obtained by boiling water flows across the heat sink. The distributions of the key heat-transfer and fluid flow parameters that result from the prediction methods described in Section 3 are shown for a mass flux of 120 kg/m^{2}s and base heat fluxes in the range 35-189 kW/m^2 in Figure 9. At a base heat flux of 35 kW/m^2, the inlet location, 12.5 mm from the inlet, is in single-phase flow with nucleation initiated before the outlet location, 37.5 mm from the inlet. This is evidenced by the significant increase in the convective heat-transfer coefficient, Figure 9a, the heat flux, Figure 9b, and the void fraction, Figure 9d. Notice that the critical void fraction is moderately above macro-scale values in this instance and that the heat flux near the onset of nucleation increases before decreasing. The increase in heat flux is caused by the increase in the heat-transfer coefficient with the decrease caused by the subsequent increase in liquid temperature as the liquid moves towards saturation. As the base heat flux increases, the onset of nucleation moves towards the heat-sink inlet and the slug critical void fraction increases. The void fraction remains at the critical value in subcooled boiling before increasing during saturated flow, Figure 9d, as assumed in the model formulation. The heat-transfer coefficient, Figure 9a, does not respond to the later increase in local void fraction, Figure 9a, as assumed in the model. Notice that the slug inception length, the length required for the void fraction to increase from 0 to the critical value, is of the order of a few millimetres, Figure 9d. At a base heat flux of 189 kW/m^2, the onset of nucleation begins at the heat-sink inlet. The large increase in the heat-transfer coefficient causes a significant distortion to the heat-flux distribution, Figure 9b, and the wall temperature, Figure 9c. The heat flux distributions in the saturated flow regions are reasonably constant, Figure 9b. In fact, for heat fluxes of 189 kW/m^2 and above, the wall inlet and outlet thermocouple locations are in a region of uniform heat flux. Figure 9b also shows the average applied heat flux, corrected for actual area and fin efficiency. The lines are of the same type as the actual distributions but are drawn in grey. The magnitude of the actual heat flux approaches the average value towards the heat-sink exit. In effect, the slug inception in the subcooled liquid produces an ‘entrance’ effect which is damped out with heat-sink length.

Typical distributions of heat-transfer and fluid flow parameters at the thermocouple inlet and outlet locations are shown for a constant mass flux and variable heat flux in Figure 10. The ‘measured’ values were obtained by assuming uniform heat flux. The ‘actual’ values were obtained from the model described in Section 3. The wall

superheat is shown to be in good agreement, Figure 10a, suggesting that the one-dimensional heat-conduction correction is not a major source of error. The heat-flux distribution, Figure 10b, shows error bars of ±11%. This is the rms deviation of the actual from the uniform heat-flux values for the data set. The 'measured' heat flux at the inlet and outlet thermocouple locations are in very good agreement with the actual values at larger heat fluxes, with most of the significant deviations occurring at low heat fluxes. The void fraction distributions are in good agreement at the outlet thermocouple where thermodynamic equilibrium is prevalent, Figure 10c. However, the effect of non-equilibrium is more pronounced at the inlet thermocouple location. These factors combine to produce the distortion to the heat-transfer coefficients shown in Figure 10d, which is relatively minor. The uniform heat flux assumption works relatively well for these flows because the heat-transfer coefficient is relatively constant across the heat sink, with distortion mainly due to slug growth and non-equilibrium effects.

Comparisons of the 'measured' and predicted values are shown in Figure 11. These show that the single mass-flux case depicted in Figure 10 is, in effect, repeated across the range, with most distortion resulting from slug growth and non-equilibrium effects, which increases with increasing mass flux. The one-dimensional heat-conduction assumption has a negligible effect on the estimation of wall superheat, Figure 11a. The heat flux at the inlet and outlet wall thermocouple locations are, in the main, reproduced by the uniform heat flux assumption, Figure 11b, with an rms error of ±10%. The heat-flux errors at the inlet and outlet location are ±13% and ±6% respectively. The errors are higher at the inlet location because they are most affected by slug growth. The discrepancies in the void fraction arise mainly from non-equilibrium effects, Figure 11c. The heat-transfer coefficient is shown to be reasonably well evaluated, Figure 11d, with an rms error of 12%. The values at the inlet and outlet thermocouple locations are ±16% and ±6% respectively, again indicating that significant errors occur close to the location of slug growth.

8.0 The uniform wall superheat model

Two common assumptions are made in heat-transfer analyses, the uniform heat-flux assumption and the isothermal wall assumption. A variant of the latter is the uniform wall superheat model. The difference between these is that the latter allows the saturation temperature to change with the evolving fluid pressure. The model outlined in Section 3 is easily modified to accommodate this assumption. An estimate of the wall superheat allows the energy equation and the heat-transfer model to be used to determine the heat-flux distribution. The wall superheat is thereafter systematically altered until the heat-flux distribution integrates to give the applied heat flux. Note that this is not synthetic data but an alternative model

The model presented in Section 3 simulates what actually happened when tests were carried out on the test piece described in Section 2. These tests showed that the wall temperatures remained reasonably constant. It was therefore reasonable to ask: Can a constant wall temperature be assumed in the analysis? The answer to this question was obtained by comparing what actually happened with what would happen if the tests were simulated by a uniform wall superheat model. The predictions are compared at the inlet and outlet wall thermocouple locations, located 12.5 and 37.5 mm from the heat-sink inlet.

Figure 4 shows a comparison between the actual and uniform wall superheat models for a typical single-phase flow. The heat-transfer coefficient is the same for both models, Figure 4a. The heat flux is overestimated near the heat-sink inlet and underestimated near the outlet, Figure 4b, as is the wall temperature, Figure 4c. The non-linear increase in liquid temperature is in reasonable agreement, Figure 4d.

Figure 12 shows the comparison between the models for all single-phase flows. The trends from Figure 4 are repeated. However, the uniform wall superheat model is in better agreement for R113 than it is for water. The wall superheat is over predicted at the inlet thermocouple location by 9% for R113 and by 22% for water. It is correspondingly under predicted at the outlet location by 7% and 13% respectively, giving overall errors of ±13%. The heat flux is predicted similarly. The inlet location heat flux is over predicted by 4% for R113 and 11% for water. The corresponding outlet location values are 7% and 20%, giving the overall errors of ±11%.

Figure 13 shows a comparison between the actual and uniform wall superheat modelling approaches for macro-scale flows (R113). The heat-transfer coefficient depends on the local gas-mass fraction, which is closely related to the void fraction, allowing the heat-transfer coefficient to change between models. Figures 13a and 13d show this to be a small effect. The predicted wall superheat has to lie in between the bounds of the actual values, which didn't vary very much. The uniform wall superheat is therefore reasonably well predicted by the approach, Figure 13b, with the uniform wall superheat values deviating by typically ±14%. The errors are more significant at low wall superheats than at larger values, in effect giving large errors from the difference of two small numbers. The heat flux results are shown in Figure 13c. The heat flux values obtained from the uniform wall superheat approach are in agreement to within ±6% of the actual values.

Figure 14 shows a comparison between the actual and uniform wall superheat modelling approaches for micro-scale flows (water). The outcome is similar to that obtained for macro-scale flows. The void fraction, Figure 14d, is not significantly different, ensuring that the heat-transfer coefficient, Figure 14a, is in agreement. The error in the wall

superheat across the heat sink is similar for these flows, ±15%, However, the heat flux estimates are not quite as good, Figure 14b, with rms errors of typically ±10%.

9.0 Discussion and conclusion

This study has shown that a uniform heat flux applied at the base of a substrate does not produce a uniform heat flux at the solid-fluid interface in single-phase flows, Figure 4b, macro-scale boiling flows, Figure 6b, or micro scale flows, Figure 9b. The type of distortion that occurs in the heat-flux distribution at the solid-fluid interface depends on the flow regime.

Single-phase flows across pin-fins have a constant heat-transfer coefficient, Figure 4a, so that the distortion, Figure 4b, results from the increasing liquid temperature, Figure 4d. The uniform heat-flux assumption is shown to be inadequate for these flows, with heat-transfer coefficients estimated by this approach being in error by typically ±22%, Figure 5d. The uniform wall superheat approach does pick up the trends in heat flux and liquid temperature quite well, Figures 4b and 4d. However, it is not sufficiently accurate to be used as a data reduction tool as the errors in estimating the heat flux are typically ±12%, Figure 12b.

Macro-scale flows have a reasonably constant saturation temperature so the distortion, Figure 6b, mainly arises from the variable heat-transfer coefficient, Figure 6a. The uniform heat-flux assumption does not work well for these flows, with estimates of the heat-transfer coefficients being in error by typically ±17%, Figure 8d. These errors may be reduced by using a uniform wall superheat model, Figure 13c. However, knowledge of the variation in heat-transfer coefficient would need to be incorporated into the analysis, as was done by McNeil et al [2].

Micro scale flows have a reasonably constant heat-transfer coefficient upstream and downstream of the onset of nucleation, Figure 9a, and a reasonably constant saturation temperature. The distortion, Figure 9b, in this case mainly arises from the rapid increase in heat-transfer coefficient caused by the slug development process, Figure 9a, and because subcooled entries were used, leading to rapid changes in temperature near the onset of nucleation. This, in effect, gives an ‘entrance’ effect that damps out with length. Sufficiently accurate results can be obtained from the uniform heat-flux assumption provided the measurement point is sufficiently downstream of the onset of nucleation, Figures 10d and 11d. Caution must be exercised in this case because the results presented are mainly for slug and elongated slug flows only. Annular flows would be expected at higher heat fluxes, where macro-type distortions are likely to occur.

The analysis of these flows suggests that distortions to the heat-flux distribution at the solid-fluid interface cannot be avoided with experiments carried out in this way. A question to pose is: Can the test section be designed to prevent these distortions? There are two factors that contribute to axial conduction in the substrate, the thermal conductivity of the substrate and its thickness. In what follows, the actual results are those obtained from the actual geometry, which contained two plates that were 5 mm thick. One plate was made from aluminium, with has a thermal conductivity of 250 W/mK, and the other was made from copper, with had a thermal conductivity of 390 W/mK, Figures 1 and 3.

The effect of the substrates thermal conductivity was assesses by altering the values used in the model described in Section 3. To complete the simulations, both plates were given the same thermal conductivity, which was systematically altered.

The results for a typical boiling macro-scale flow (R113) are shown in Figure 15. The heat flux distribution for the actual material, copper and aluminium, is similar to that achieved when the wall thermal conductivity was set to 250 W/mK, Figure 15a. Both of these results are consistent with the applied heat flux (ideal). A more uniform heat flux was achieved when the wall thermal conductivity was set to 25 and 2.5 W/mK. However, they are significantly above the ideal value. This occurred because the heat flux has two heat paths, one through the base and one through the pin-fins, as described by Equation (13), which can be re-written as,

$$q_b = q_s A^+ \tag{34}$$

where A^+ is the effective area ratio, defined as the ratio of the heat-transfer surface to the base area, i.e.

$$A^+ = 1 + \frac{\left(4\eta H_{ch} W_w - W_w^2\right)}{\left(W_{ch}^2 + W_w^2\right)^2} \tag{35}$$

The effective area ratio becomes the geometric area ratio when the fine efficiency is unity. The geometric ratio is 1.75 for the surface used, Figure 2. The path through the pin fin becomes less effective as the thermal conductivity deceases, Equations (14) and (15). This is demonstrated in Figure 15b. Thus, a large wall thermal conductivity is required for the extended surface to be useful and a uniform heat flux cannot be achieved with a large wall thermal conductivity.

Simulations for a typical boiling micro-scale flow (water) are presented in Figure 16. The spike in the heat flux at the heat sink inlet is shown to be diminished by decreases in the wall thermal conductivity, Figure 16a. However, the extended surface is again rendered ineffective, Figure 16b.

The effect of substrate thickness was assessed in a similar manner, with the total wall thickness altered while maintaining half of that thickness as copper and the other half as aluminium. Typical results for macro-scale flows

(R113) are shown in Figure 17. As the thickness is decreased the effective area ratio is maintained, Figure 17b, and the heat flux becomes more uniform, Figure 17a. However, even at a thickness of 1 mm, the same magnitude as the height of the extended surface, a uniform heat flux is not achieved, with significant distortions visible near the inlet and outlet of the heat sink. The exercise is repeated for micro-scale flows (water) in Figure 18. Again the effective area ratio is maintained, Figure 18b. However, the reduction in substrate thickness does not diminish the spike in the heat flux at the heat-sink inlet, Figure 18a. Thus, reducing the substrate thickness is effective, but not effective enough.

The analyses undertaken to evaluate the validity of the uniform heat flux assumption, Figures 6-11, show that it can lead to significant errors in the measurement of the heat-transfer coefficient. The uniform wall superheat assumption may improve things, but not sufficiently, Figures 12-14. Simulations, Figures 15-18, have demonstrated that limited scope exists for improving these measurements through test-section design. It therefore seems likely that future experiments carried out using this approach will require much more detailed wall temperatures to be obtained. This would allow the actual heat-flux distribution at the solid-fluid interface to be obtained from the solution of the wall conduction equation, solved in three dimensions with measured boundary conditions. Such a possibly could be realised by using infra-red camera temperature measurement techniques, as suggested by Szczukiewicz et al [3].

References

[1] McNeil D A, Raeisi A H, Kew P A and Hamed R S, 2013. Flow boiling heat-transfer in micro to macro transition flows. Int. J. Heat Mass Transfer, 65, 289-307.

[2] McNeil D A , Raeisi A H, Kew P A and Hamed R S. An investigation into flow boiling heat transfer and pressure drop in a pin-finned heat sink. Submitted for publication.

[3] Szczukiewicz S, Magnini M and Thome J R, 2014. Proposed models, ongoing experiments and latest numerical simulations of microchannel two-phase flow. Int J Multiphase Flow, 59, 88-101.

[4] McNeil D A, Raeisi A H, Kew P A and Bobbili P R. A comparison of flow boiling heat-transfer in in-line mini pin fin and plane channel flows. Appl. Therm. Eng. 30 (2010) 2412-2425.

[5] Sato T and Matsumurs H, 1963. On the condition of incipient subcooled boiling and forced convection. Bull JSME, 392-398.

[6] ESDU, 1979. Crossflow Pressure Loss over Banks of Plain Tubes in Square and Triangular Arrays Including Effects of Flow Direction. Engineering Sciences Data Unit, Item 79034.

[7] Ishihara K, Palen J W and Taborek J, 1980. Critical review of correlations for predicting two-phase flow pressure drop across tube banks. Heat Transfer Eng, 1, 23-32.

[8] Cooper M G, 1984. Heat Flow Rates in Saturated Nucleate Pool Boiling - A Wide Ranging Examination Using Reduced Properties. Advances in Heat Transfer, Academic Press, Orlando, 16, 157-239.

[9] Taitel, Y and Dukler A E, 1976, A model for predicting flow regimes in horizontal and near horizontal gas-liquid flow, AICHE J, 22, pp 47-55.

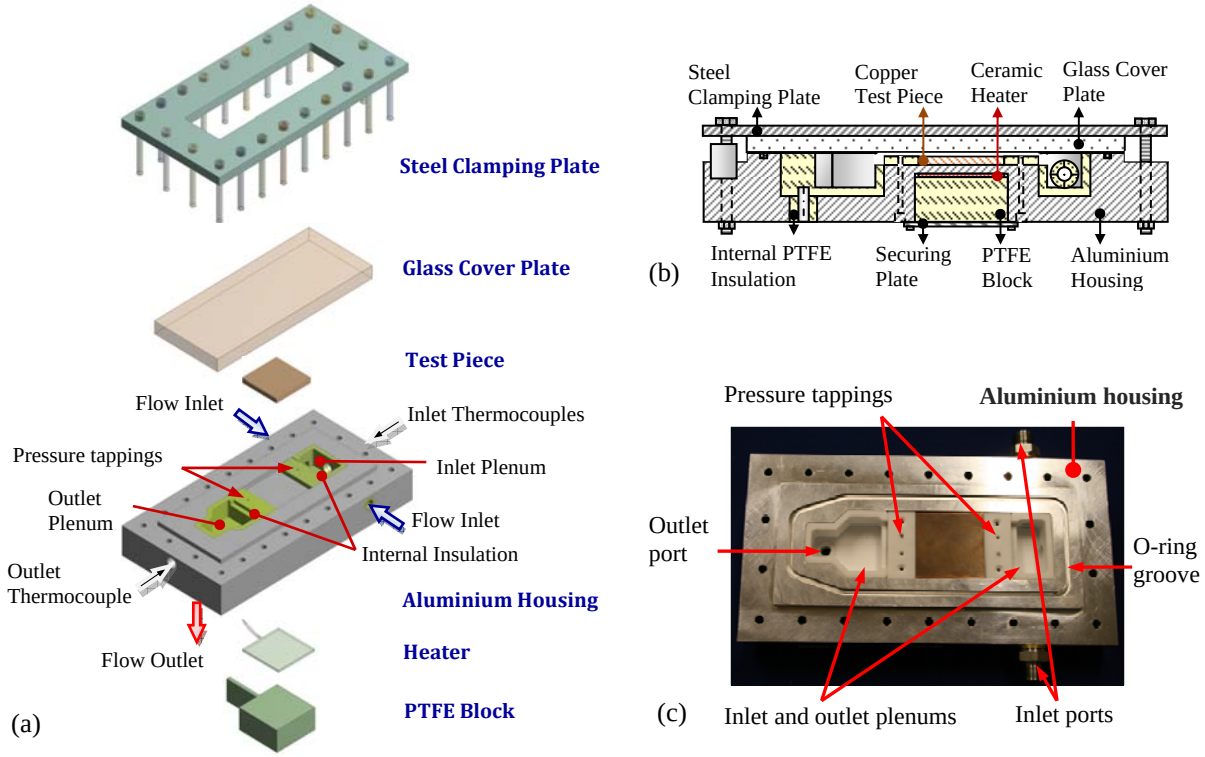

Figure 1: (a) Test section construction, (b) Longitudinal cross-section of the test section assembly with internal insulation, (c) Test section open view with internal insulation

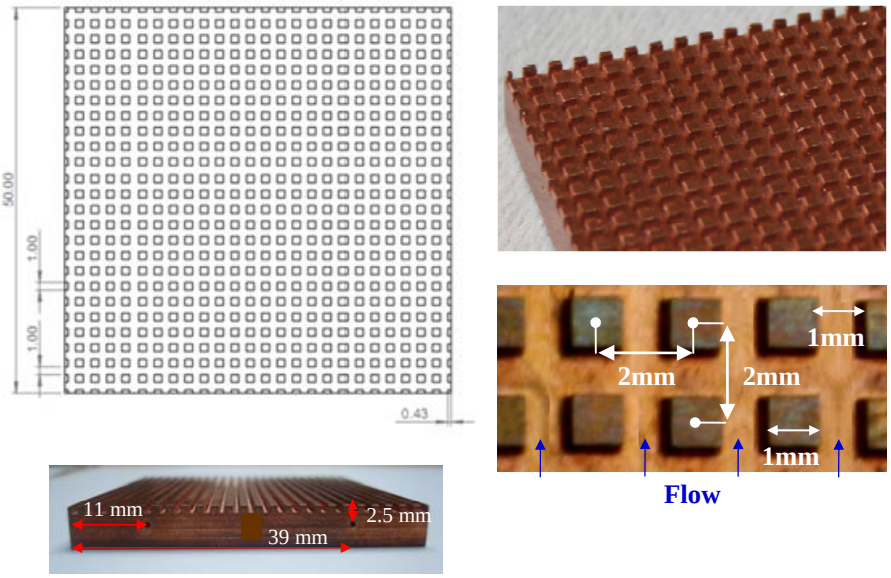

Figure 2: In-line pin-fin test piece

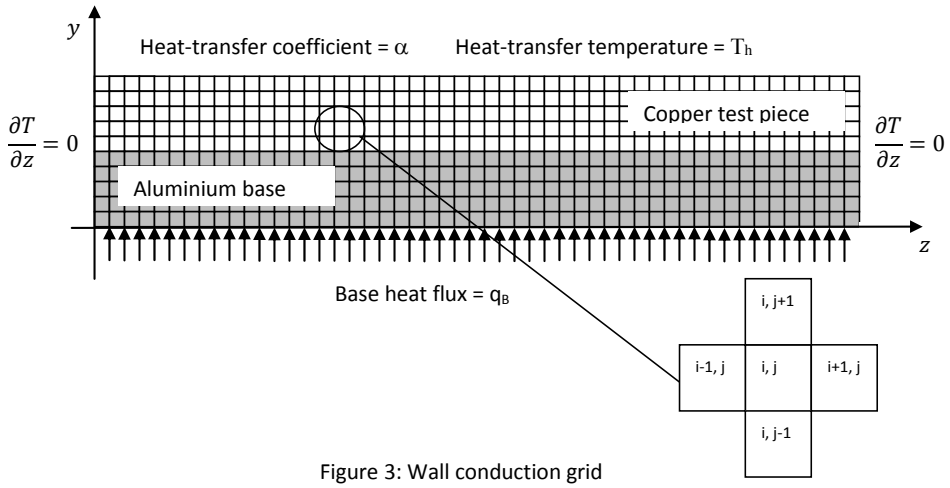

Figure 3: Wall conduction grid

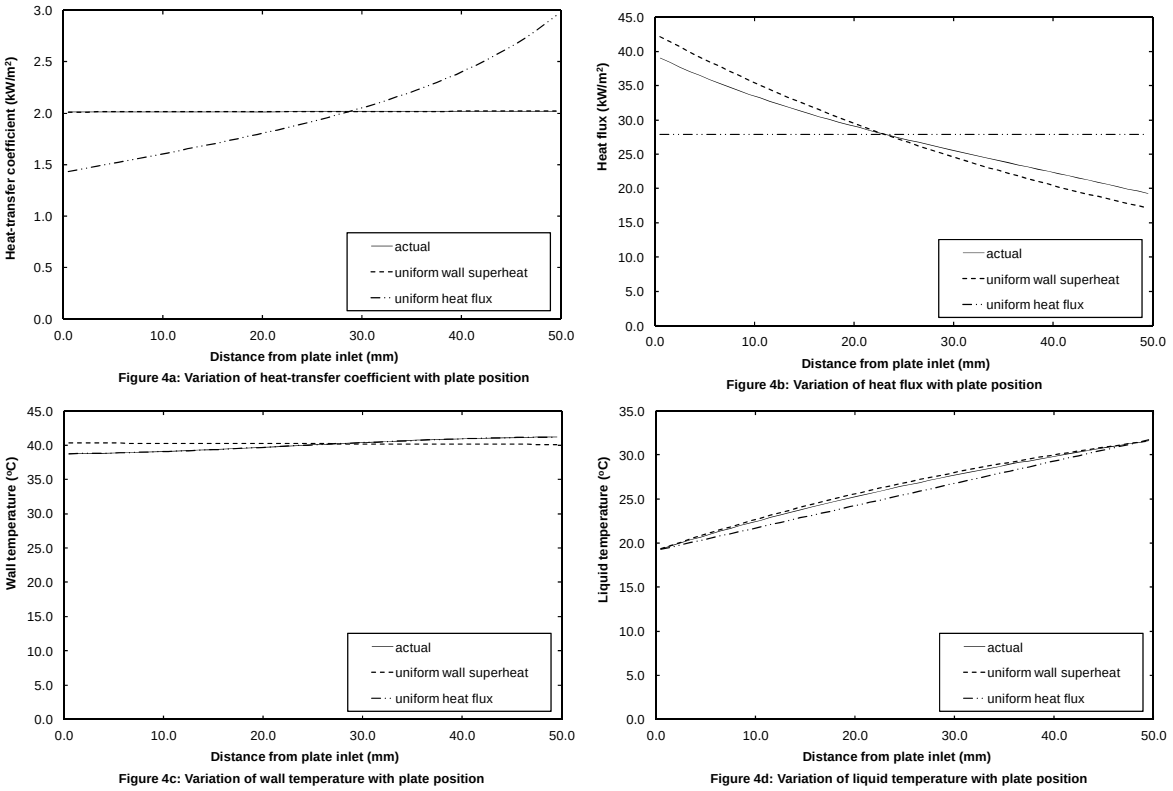

Figure 4a: Variation of heat-transfer coefficient with plate position

Figure 4b: Variation of heat flux with plate position

Figure 4c: Variation of wall temperature with plate position

Figure 4d: Variation of liquid temperature with plate position

Figure 4: Single-phase distributions

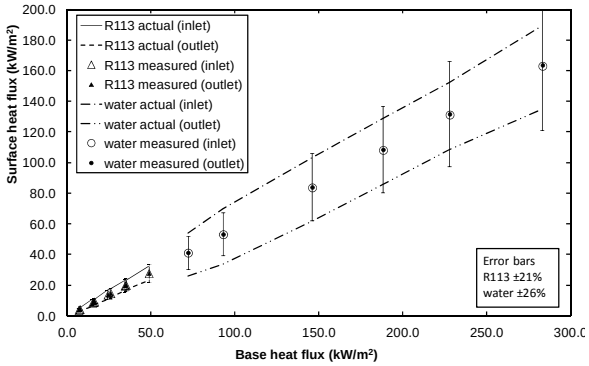

Figure 5a: Variation of surface with applied heat flux

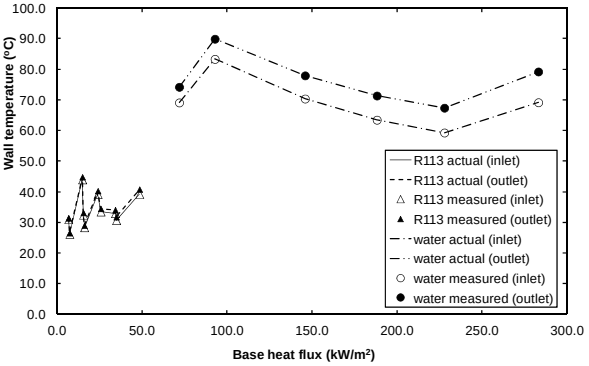

Figure 5b: Variation of wall temperature with applied heat flux

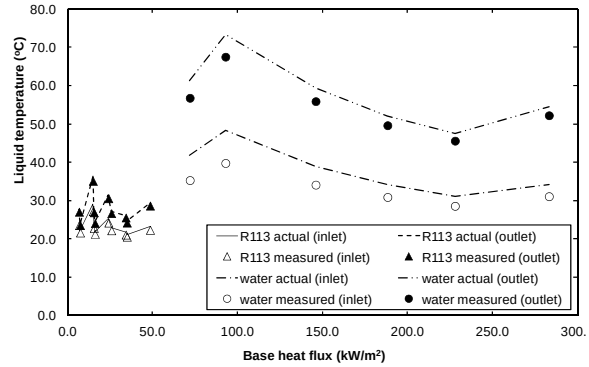

Figure 5c: Variation of liquid temperature with applied heat flux

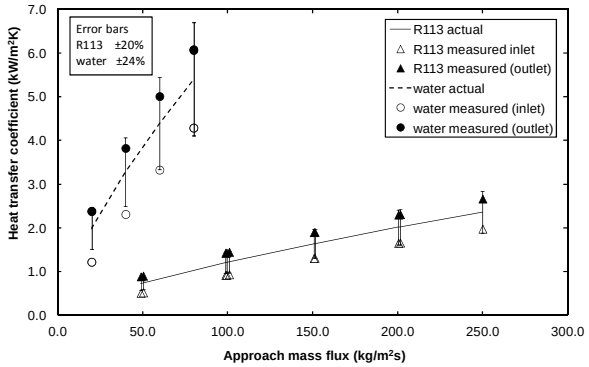

Figure 5d: Variation of heat transfer coefficient with mass flux

Figure 5: Single-phase results

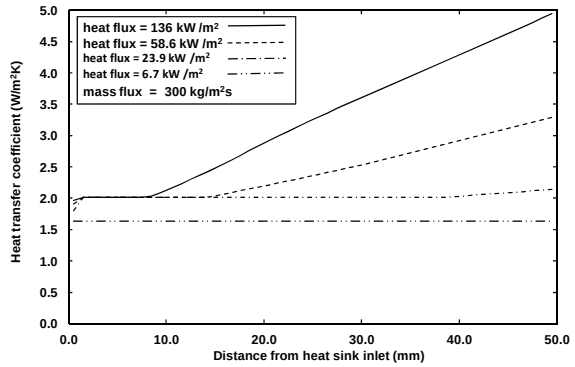

Figure 6a: Variation of heat transfer coefficient with heat sink position

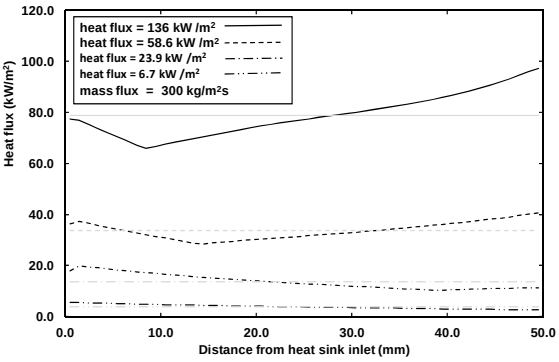

Figure 6b: Variation of heat flux with heat sink position

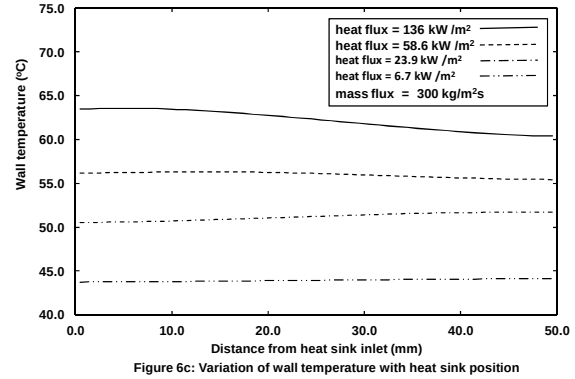

Figure 6c: Variation of wall temperature with heat sink position

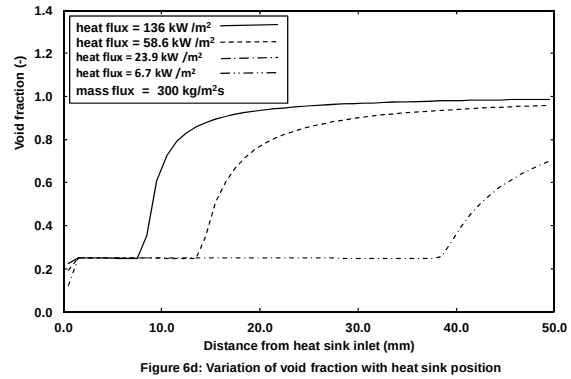

Figure 6d: Variation of void fraction with heat sink position

Figure 6: Typical distributions of boiling parameters for R113

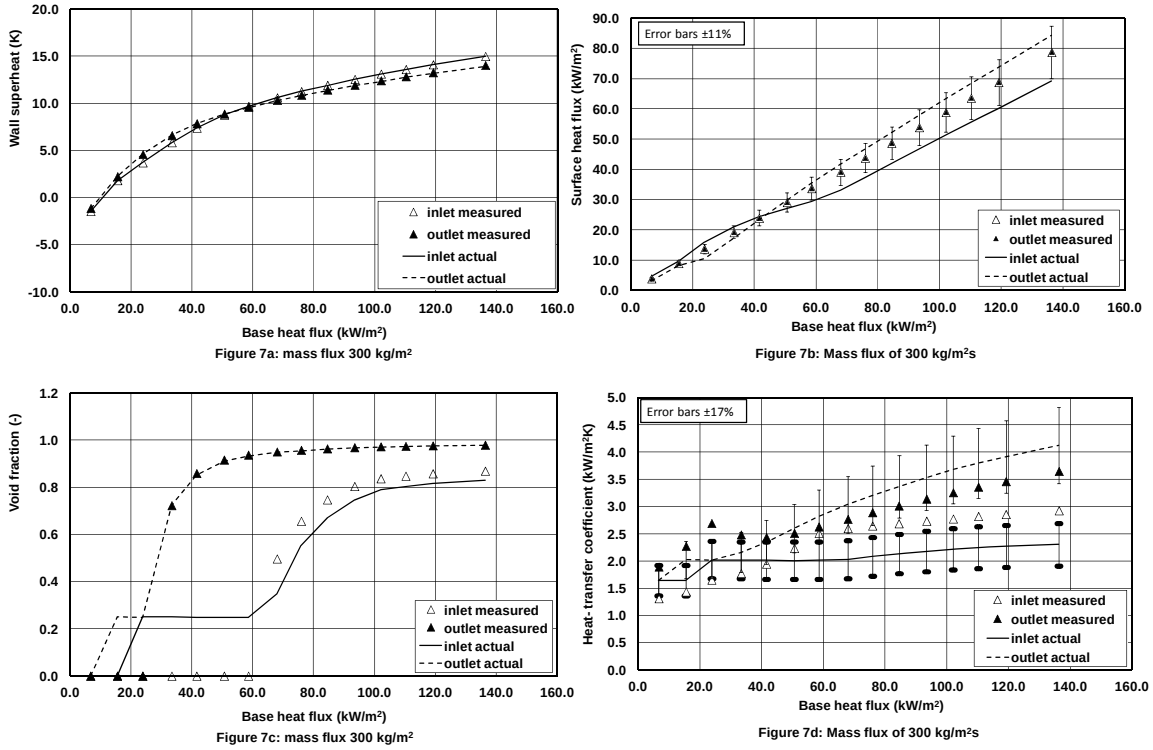

Figure 7: Typical response of R113 Boiling parameters to changing heat flux

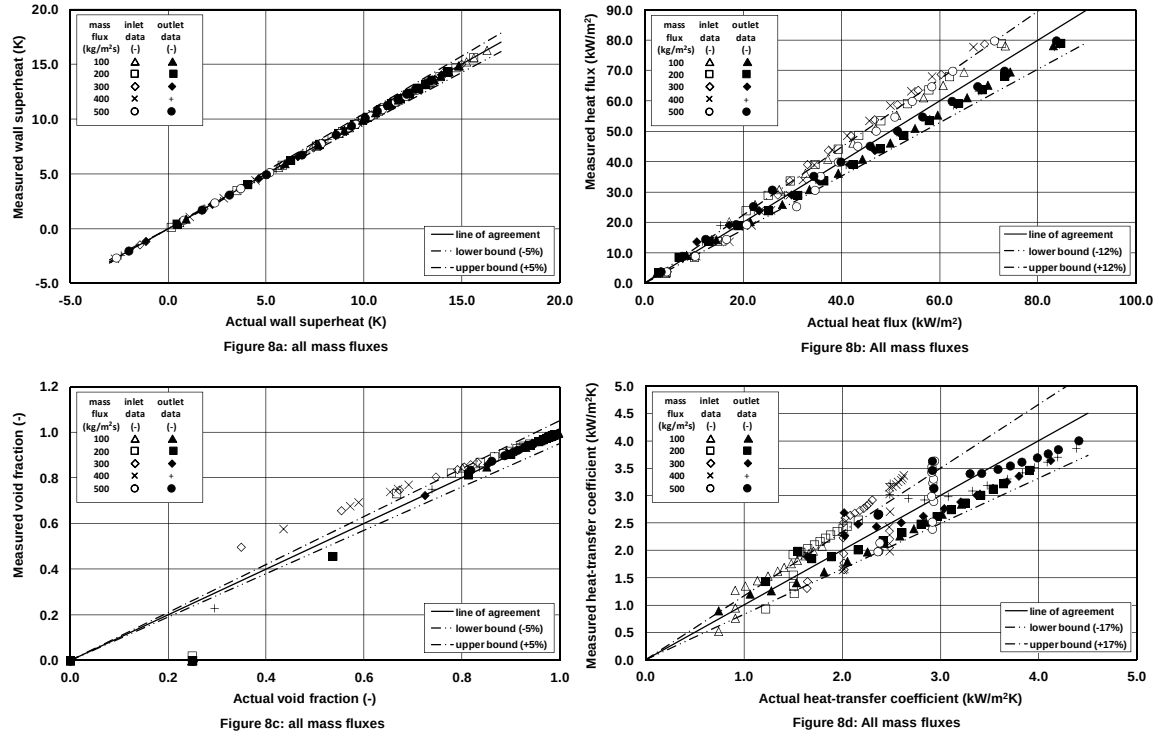

Figure 8: Comparison of Boiling R113 parameters with the uniform heat flux values

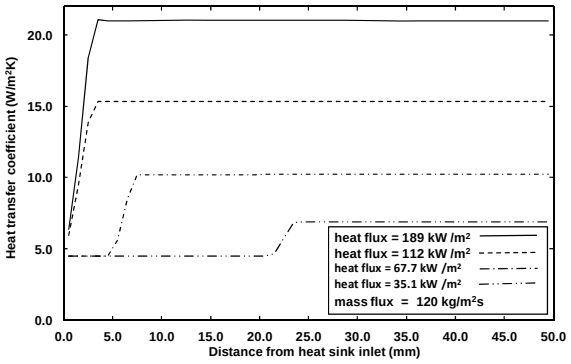

Figure 9a: Variation of heat transfer coefficient with heat sink position

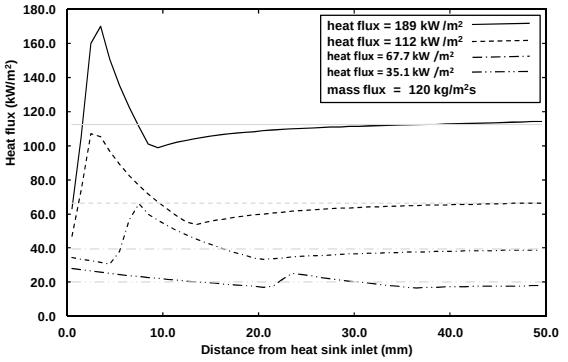

Figure 9b: Variation of heat flux with heat sink position

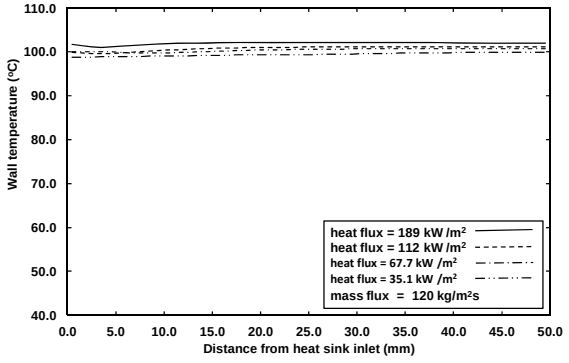

Figure 9c: Variation of wall temperature with heat sink position

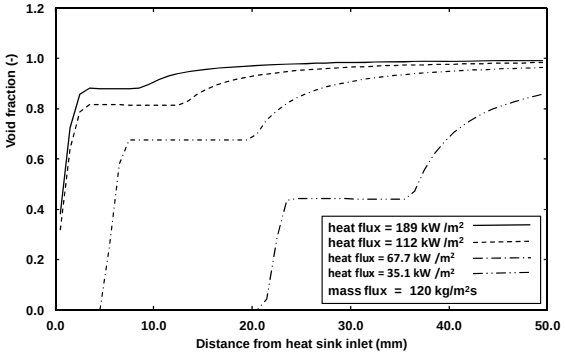

Figure 9d: Variation of void fraction with heat sink position

Figure 9: Typical distributions of boiling parameters for water

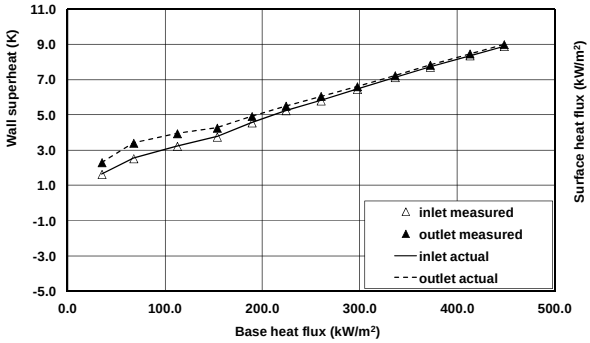

Figure 10a: mass flux 120 kg/m²

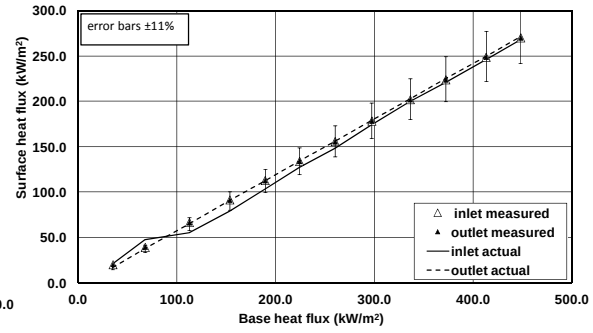

Figure 10b: Mass flux of 120 kg/m²s

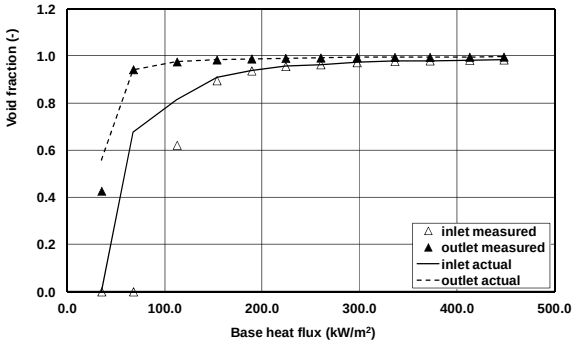

Figure 10c: mass flux 120 kg/m²

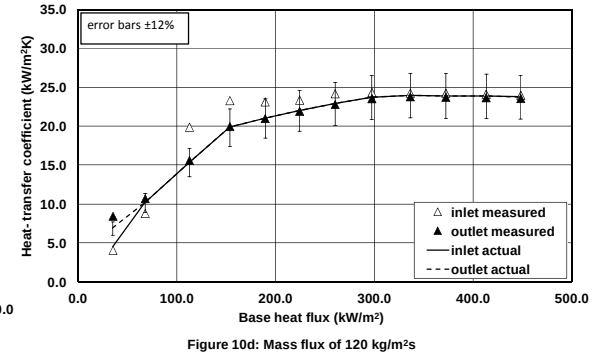

Figure 10d: Mass flux of 120 kg/m²s

Figure 10: Typical water boiling parameters response to changes in heat flux

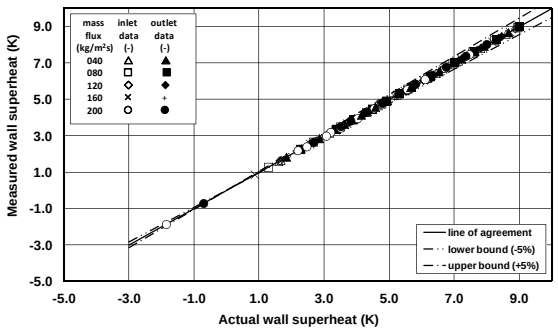

Figure 11a: all mass fluxes

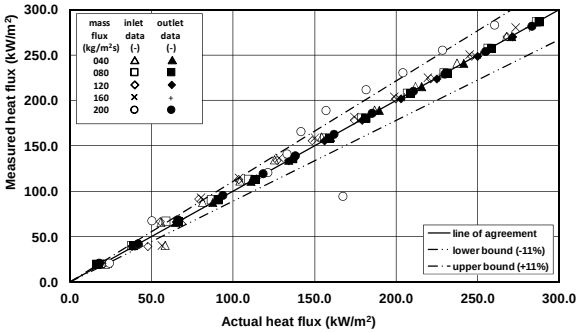

Figure 11b: All mass fluxes

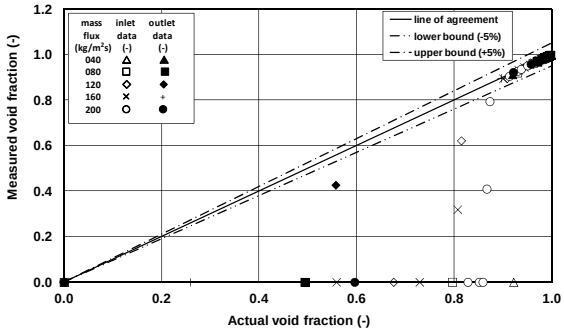

Figure 11c: all mass fluxes

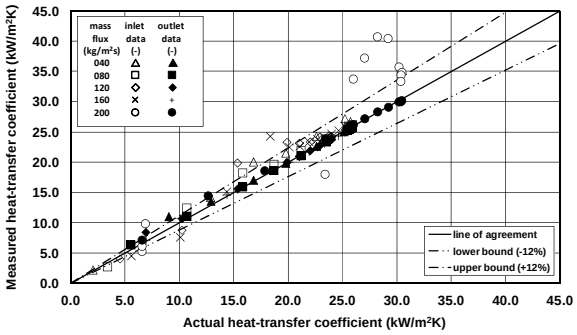

Figure 11d: All mass fluxes

Figure 11: Comparison of boiling water parameters with the uniform heat flux values

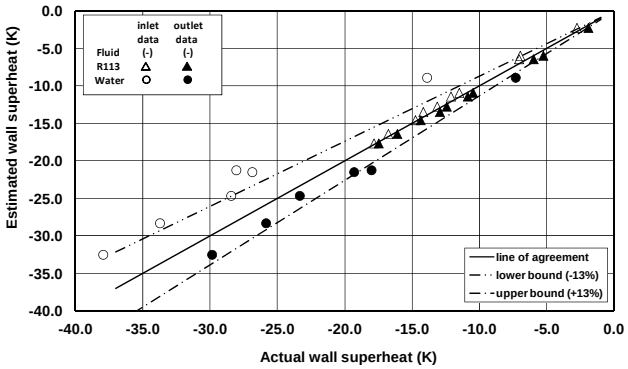

Figure 12a: Comparison of uniform with actual wall superheats for single-phase flows

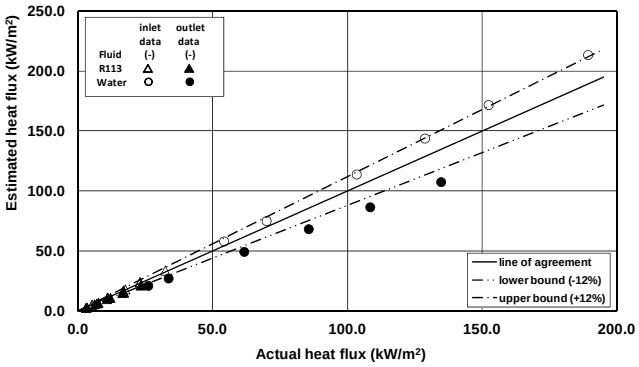

Figure 12b: Comparison of uniform wall superheat with actual heat fluxes for single-phase flows

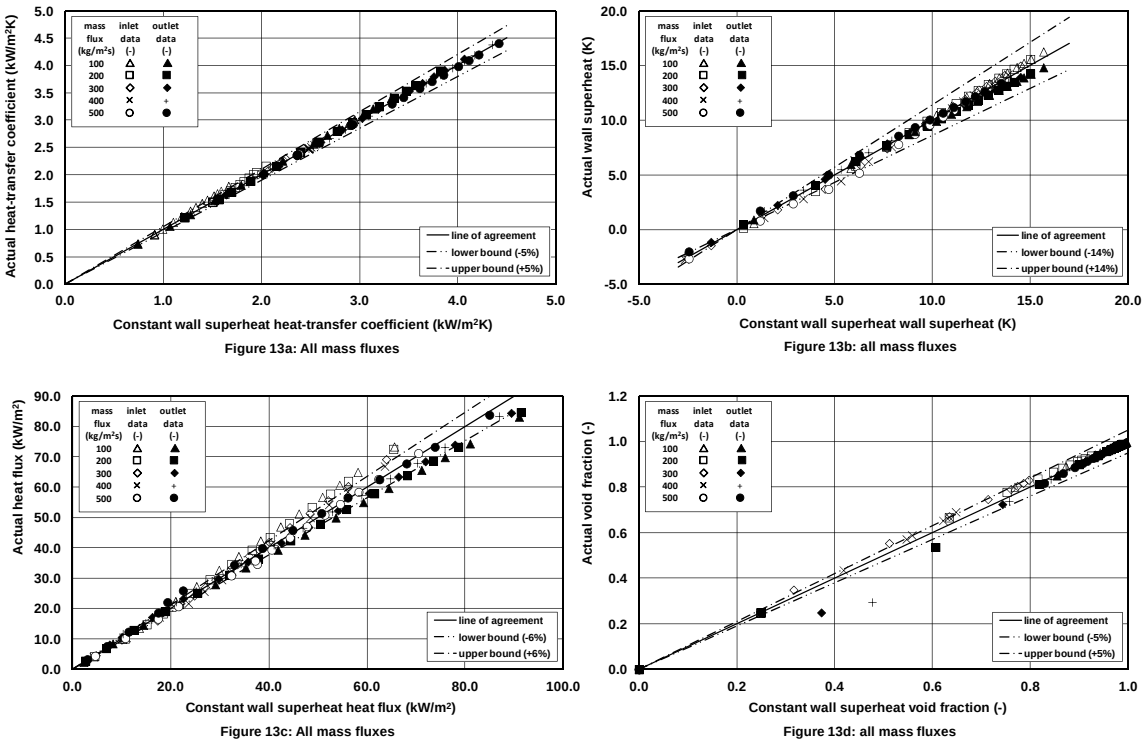

Figure 13a: All mass fluxes

Figure 13b: all mass fluxes

Figure 13c: All mass fluxes

Figure 13d: all mass fluxes

Figure 13: Comparison of boiling R113 parameters with the uniform wall superheat values

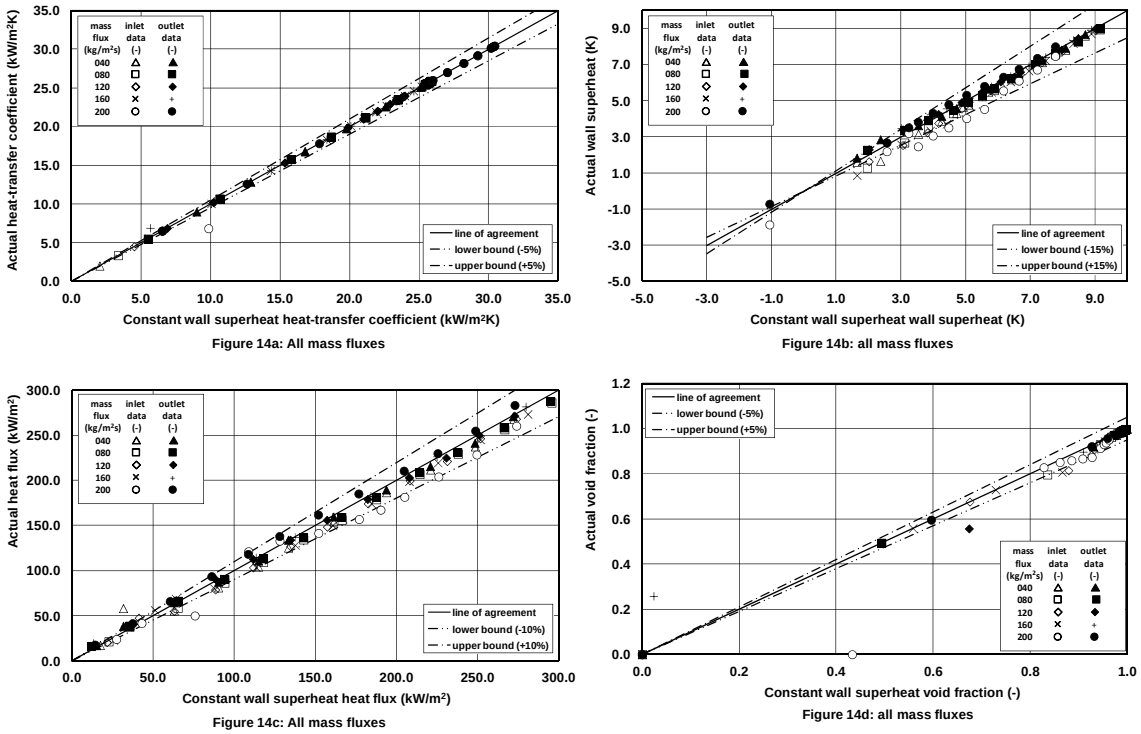

Figure 14a: All mass fluxes

Figure 14b: all mass fluxes

Figure 14c: All mass fluxes

Figure 14d: all mass fluxes

Figure 14: Comparison of boiling water parameters with the uniform wall superheat values

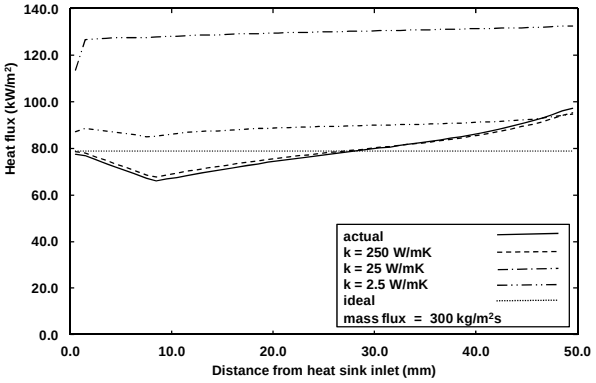

Figure 15a: Variation of heat flux with heat sink position for R113

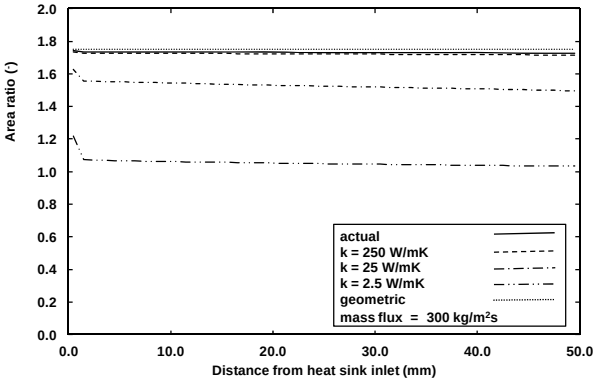

Figure 15b: Variation of area ratio with heat sink position for R113

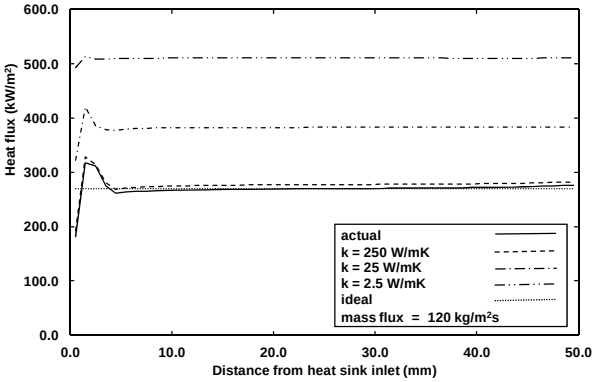

Figure 16a: Variation of heat flux with heat sink position for water

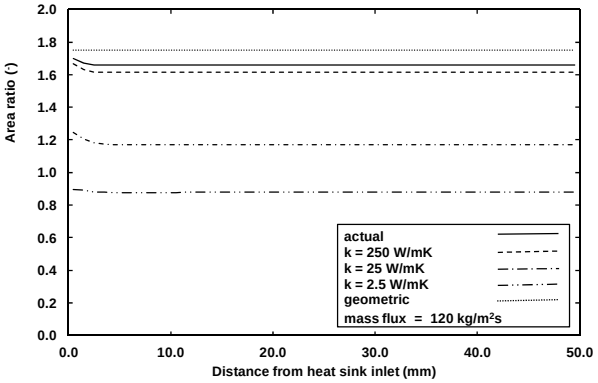

Figure 16b: Variation of area ratio with heat sink position for water

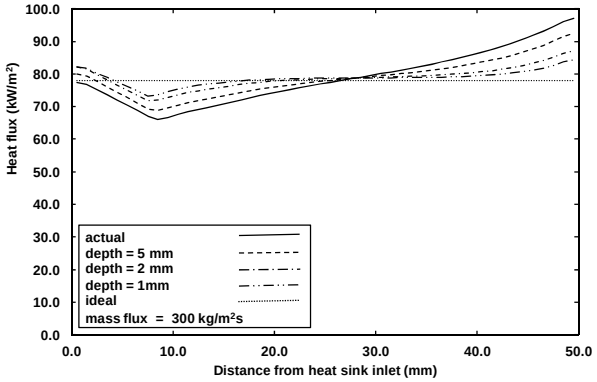

Figure 17a: Variation of heat flux with heat sink position for R113

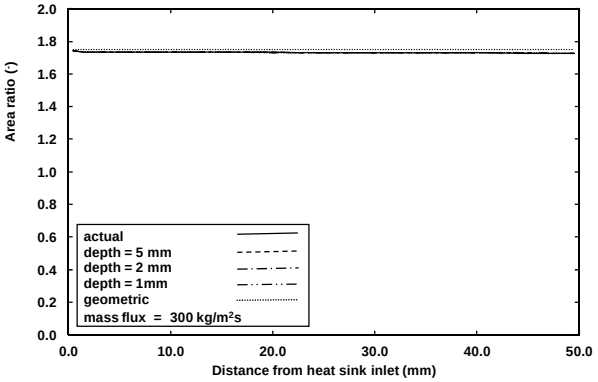

Figure 17b: Variation of area ratio with heat sink position for R113

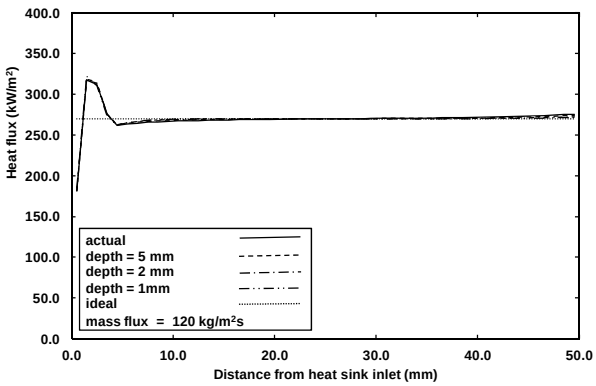

Figure 18a: Variation of heat flux with heat sink position for water

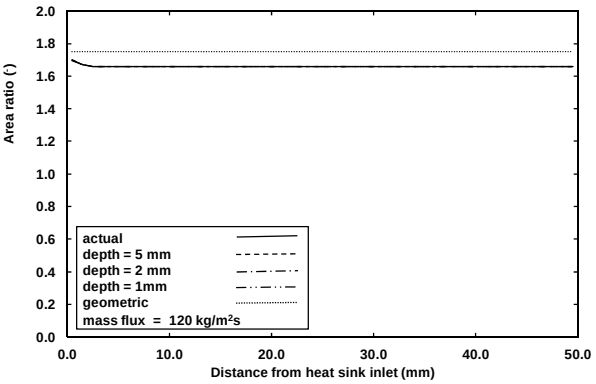

Figure 18b: Variation of area ratio with heat sink position for water